Petroleum Science 20 (2023) 3240–3250

Contents lists available at ScienceDirect

Petroleum Science

journal homepage: www.keaipublishing.com/en/journals/petroleum-science

Original Paper

New insights into the mechanism of reactive adsorption desulfurization on Ni/ZnO catalysts: Theoretical evidence showing the existence of interfacial sulfur transfer pathway and the essential role of hydrogen

Hou-Yu Zhu [a, *], Nai-You Shi [a], Dong-Yuan Liu [a], Rui Li [a], Jing-Gang Yu [a], Qi-Tang Ma [a], Tu-Ya Li [a], Hao Ren [a], Yuan Pan [b], Yun-Qi Liu [b, **], Wen-Yue Guo [a, ***]

[a] School of Materials Science and Engineering, China University of Petroleum (East China), Qingdao, 266580, Shandong, China
[b] State Key Laboratory of Heavy Oil Processing, College of Chemistry and Chemical Engineering, China University of Petroleum (East China), Qingdao, 266580, Shandong, China

ARTICLE INFO

Article history:
Received 22 November 2022
Received in revised form
19 January 2023
Accepted 19 May 2023
Available online 22 May 2023

Edited by Jia-Jia Fei

Keywords:
Reactive adsorption desulfurization
Ni/ZnO
Interface
Sulfur transfer
Density functional theory

ABSTRACT

As well known in the petroleum industry and academia, Ni/ZnO catalysts have excellent desulfurization performance. However, the sulfur transfer mechanism of reactive adsorption desulfurization (RADS) that occurs on Ni/ZnO catalysts remains controversial. Herein, a periodic Ni nanorod supported on ZnO slab was built to represent the Ni/ZnO system, and density functional theory calculations were performed to study the sulfur transfer process and the role of H_2 within the process. The results elucidate that the direct solid-state diffusion of S from Ni to interfacial oxygen vacancies (O_v) is more favorable than the hydrogenation of S to SH/H_2S on Ni and the subsequent H_2S desorption, and accordingly, H_2O is produced on Ni rather than on ZnO. Ab initio thermodynamics analysis shows that the hydrogen atmosphere applied in preparing Ni/ZnO catalysts greatly promotes the O_v formation on ZnO surface, which accounts for the presence of interfacial O_v in freshly prepared catalysts. Under RADS condition, hydrogenation of interfacial O atoms to form O–H groups facilitates the reverse spillover of these lattice O atoms from ZnO to Ni, accompanied with the interfacial O_v generation. In contrast to the classic S transfer mechanism via H_2S, the present work clearly demonstrates that the interfacial S transfer is a feasible reaction pathway in the RADS mechanism. More importantly, the existence of interfacial O_v is an essential prerequisite for this interfacial S diffusion, and H_2 plays a key role in facilitating the O_v formation.

1. Introduction

Among current desulfurization technologies for transportation fuels, the reactive adsorption desulfurization (RADS), represented by a S-Zorb process (Huang et al., 2011; Huang et al., 2013) industrialized by Conoco Philips Petroleum Co., has gained increasing attention due to the advantageous features of lower hydrogen consumption and negligible loss of octane number compared with the conventional hydrodesulfurization approach (Gislason, 2001; Jiang et al., 2021; Kang et al., 2020; Khare, 2001, 2004; Liu et al., 2023; Meng et al., 2014; Wang et al., 2022; Yan et al., 2022). Ni/ZnO is the main part of desulfurization catalyst in S-Zorb. Ni acts as desulfurization center, and removed sulfur atoms are transferred from Ni to ZnO, which adsorbs sulfur and converts into ZnS (Babich and Moulijn, 2003; Tawara et al., 2000). S transfer from Ni to ZnO is important for RADS because sulfurized Ni surface must be restored to maintain the desulfurization activity. Despite intense research efforts on the RADS mechanism (Babich and Moulijn, 2003; Huang et al., 2010; Zhang et al., 2017), some fundamental arguments are still not clear, especially for the sulfur transfer pathway and the vital role of hydrogen. An atomistic understanding of sulfur transfer process is essential for the

* Corresponding author.
** Corresponding author.
*** Corresponding author.
E-mail addresses: hyzhu@upc.edu.cn (H.-Y. Zhu), liuyq@upc.edu.cn (Y.-Q. Liu), wyguo@upc.edu.cn (W.-Y. Guo).

https://doi.org/10.1016/j.petsci.2023.05.014

design of Ni/ZnO-based catalysts and relevant desulfurization processes with enhanced reactivity.

The classic S transfer mechanism in RADS includes thiophene desulfurization on Ni, hydrogenation of removed S to H_2S followed by H_2S desorption from Ni, and ZnO adsorption of H_2S and conversion to ZnS accompanied with H_2O formation and desorption from ZnO (Babich and Moulijn, 2003; Bezverkhyy et al., 2008; Huang et al., 2010, 2011; Ryzhikov et al., 2008; Tang et al., 2019; Ullah et al., 2017; Zhang et al., 2012; Zhao et al., 2018). It's a widely held belief that H_2 plays a prominent role in transforming S to H_2S and preserving Ni in a reduced state, because a rapid deactivation occurs in the absence of H_2 in the feed stream (Huang et al., 2011; Song et al., 2021; Zhao et al., 2018). However, controversies over gas-phase S transfer via H_2S have risen as H_2S was not detected in the exit stream, and direct solid-state S diffusion seems to be more efficient for S transfer (Gupta et al., 2016; Song et al., 2021). Gupta et al. (2016) reported high-performance catalysts containing Ni clusters on ZnO nanowire. As evidenced by the XPS, TEM and XRD results, ZnS but no NiS phase was observed in the spent catalyst, supporting the RADS mechanism in which the Ni active center is recovered. They attributed the absence of NiS to the effective S transfer from sulfurized Ni cluster to ZnO nanowire and then assumed that the likely sulfur transfer mechanism involves solid-state pathway via the Ni/ZnO interface. Song et al. (2021) recently prepared Ni_3S_2/ZnO by mechanical mixing and exposed the mixture to nitrogen and hydrogen separately. Through comparative experiments, they concluded that efficient S transfer could be achieved at the Ni/ZnO interface, and more importantly, H_2 atmosphere is essential for the sulfur transfer. The conclusion of the above experimental research raises two key questions: (1) how does the solid-state diffusion of S between Ni and ZnO occur? and (2) how does H_2 get involved in the solid-state S transfer? Clarifying these fundamental arguments is, however, unlikely because of the limitations of current experimental techniques. Therefore, carrying out a detailed theoretical investigation is important for obtaining deep insights on such RADS process.

The common sense of S transfer via gas-phase H_2S is also inconsistent with theoretical results by density functional theory (DFT) calculations (Ji et al., 2012; Zhang et al., 2012). Ji et al. (2012) found that the formation of H_2S on Ni(100) is difficult due to the high hydrogenation barrier of 3.60 eV involved. Zhu et al. (2021) recently performed a DFT study of thiophene desulfurization and conversion of desulfurization products on Ni(111) surface and Ni_{55} cluster. Different from the classic gas-phase S transfer via H_2S, the results showed that direct diffusion of S on Ni substrate is more favorable than the hydrogenation of S to H_2S. Zhang et al. (2012) used a Zn_3NiO_4 cluster to represent Ni/ZnO catalysts and proposed that direct transfer of S from Ni to Zn site is preferred to H_2S formation path. It's oversimplified to use a certain crystal surface of Ni or the Zn_3NiO_4 cluster as representative of Ni/ZnO catalysts. Thus, an appropriate Ni/ZnO model is required for exploring the S transfer mechanism and providing more detailed information on the elementary reaction steps. In addition, previous DFT works on H_2S–ZnO interaction revealed that H_2O formation via the combination of two surface O–H groups is generally not easy due to a high energy barrier of approximately 2 eV for breaking one O–H bond (Li et al., 2022; Ling et al., 2013; Zhao et al., 2018). The difficulty in producing H_2O on ZnO leads to questioning the consensus of H_2S adsorption and H_2O formation on ZnO during the RADS process. There should be a more feasible pathway to generate H_2O. However, up to now, no theoretical research has been reported to illustrate how H_2O is generated on Ni/ZnO catalysts.

Here, a comprehensive study on the S transfer process of Ni/ZnO catalysts was performed by DFT calculations to tackle the above issues. The main focus is to clarify the possible reaction steps that occur between the deposition of removed S on Ni active center and the formation of stable Zn–S bond. The structures and energies for S adsorption were addressed, the elementary reactions for initial hydrogenation and surface diffusion of S on Ni nanorod were investigated, and detailed potential energy surfaces (PESs) of the S transfer mechanism that occurred along the Ni/ZnO interfacial boundary were presented. In addition, the formation of interfacial oxygen vacancy (O_v) and H_2O was discussed.

2. Computation details

2.1. Computational methods

The Vienna ab initio simulation package (VASP) (Kresse and Furthmüller, 1996a, 1996b) was used to conduct DFT calculations. The projector augmented wave (PAW) (Blöchl, 1994; Kresse and Joubert, 1999) was employed to describe interactions between core and valence electrons. Electron exchange and correlation were treated within the generalized gradient approximation developed by Perdew, Burke, and Ernzerhof (GGA-PBE) (Kresse and Furthmüller, 1996a, 1996b; Perdew et al., 1996). Plane waves were included for the electronic wave functions up to a cutoff energy of 400 eV. The convergence criteria were set to 10^{-6} eV and 0.03 eV/Å for the energy and force, respectively. All computations were performed with spin polarization.

The lattice constants of bulk Ni and ZnO were fitted by the Birch–Murnaghan equation of state using 15 × 15 × 15 and 15 × 15 × 10 *k*-point meshes, respectively. The calculated lattice constant of Ni is 3.521 Å, in accordance with the experimental value (3.524 Å) (Suh et al., 1988). The lattice constants of ZnO were calculated as $a = b = 3.297$ Å and $c = 5.296$ Å, in agreement with the experimental values of $a = b = 3.249$ Å and $c = 5.204$ Å (Karzel et al., 1996). The above computed lattice constants were subsequently applied in all calculations.

Transition state (TS) searches were performed using the climbing-image nudged elastic band (CINEB) method (Henkelman and Jónsson, 1999; Henkelman et al., 2000) and confirmed by the existence of one imaginary frequency along the reaction coordinate. The energy barrier (E_a) was determined as the energy difference between the corresponding TS and the adsorbed initial state (IS), and the reaction energy (E_r) was defined as the energy difference between the final state (FS) and IS.

The Gibbs free energy change (ΔG) of each reaction step is given by

$$\Delta G = \Delta E + \Delta E_{ZPE} - T\Delta S \quad (1)$$

where ΔE, ΔE_{ZPE}, and ΔS are the differences in total energy, zero-point energy, and entropy, respectively. T, the reaction temperature, was set to 673.15 K in this work. In the calculation of ZPE and vibrational entropy, only the adsorbates were allowed to relax in frequency calculations. Entropies of gas molecules, such as H_2, were taken from standard values (Johnson, 2016).

2.2. Computational models

Periodic Ni nanorod (Ni_{nr}) supported on ZnO slab was constructed to represent the Ni/ZnO system, as shown in Fig. 1. The Ni nanorod was chosen because this periodic nanorod model provides a steady Ni/ZnO interface structure, which is helpful in researching for solid-state pathway of S transfer. For comparison, another type of metal/oxide model is oxide-supported clusters, such as $Ni_{2\text{-}7,13}/\gamma\text{-}Al_2O_3$ (Liu et al., 2014; Silaghi et al., 2016) and $Pt_{7,8,13}/\gamma\text{-}Al_2O_3$ (Mager-Maury et al., 2011; Sun et al., 2019; Zhai and Alexandrova, 2018; Zhao et al., 2019). The structures of these nonperiodic

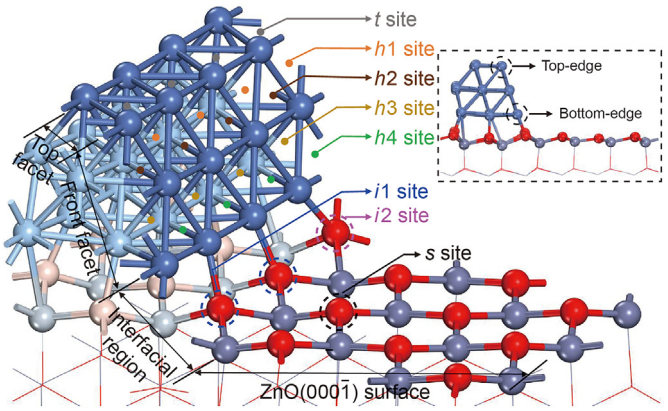

Fig. 1. Oblique view of the Ni_{nr}/ZnO model. Side view is given in small illustration. Different sites on top and front facets of Ni_{nr}, interfacial region and ZnO surface are labeled. The Ni, Zn, and O atoms are colored with dark blue, silver gray, and red, respectively. Only the top bilayer (O–Zn) of ZnO slab is shown for clarity, and the light blue color is applied for the Ni atoms behind the front facet and below the top facet of the Ni nanorod.

clusters are fluxional and subjected easily to the temperture and reactants, and they are not the appropriate models to quantitatively characterize the interfacial properties of metal/oxide systems. Zhu et al. (2019) recently employed a periodic Pt_{nr}/α-Al_2O_3 model to simulate the C–S bond cleavage of methanthiol along interfacial active sites. Similar models, such as Au_{nr}/CeO_2, have also been used by Green et al. (2011) and Song et al. (2014) to study the interfacial CO oxidation mechanisms.

An O-terminated ZnO(000$\bar{1}$) slab with a "3 × 6" surface supercell was built as the substrate to support Ni_{nr}, consisting of eight atomic layers or four "O–Zn" bilayers and a vacuum space of 16 Å. The construction details for the "3 × 6" ZnO slab are shown in Fig. S1 of the Electronic Supplementary Material (ESM). The ZnO(000$\bar{1}$) surface was chosen because it is the most stable and common ZnO surface (Duan et al., 2018). In all calculations, the bottom four atomic layers of the slab were kept fixed at their bulk-like position, whereas the remaining atoms in the top four atomic layers as well as the Ni_{nr} and adsorbed intermediates, were allowed to relax. Then, a three-layer Ni_{nr} was added on the ZnO surface, which consists of three, three, and two Ni rows per layer. The 3 × 1 × 1 *k*-point meshes were used for the Ni_{nr}/ZnO(000$\bar{1}$) model. The Ni_{nr} was found to be stably located above the surface O sites, and the top and front facets of the Ni_{nr} are (111) facets, as shown in Fig. 1. The Ni(111) was chosen because it was identified as the thermodynamically most stable surface of bulk Ni in X-ray diffraction experiments (Kumar and Chakarvarti, 2004). Five types of adsorption sites on the Ni_{nr} were considered, i.e., top site (*t*) on the top facet of Ni_{nr} and hollow sites (*h*1–*h*4) on the front facet of Ni_{nr}. The *h*1–*h*4 sites were located in sequence from the top-edge to the bottom-edge of Ni_{nr} (Fig. 1). Along the interfacial boundary of Ni_{nr}/ZnO two types of oxygen sites were exposed, labeled as the *i*1 and *i*2 sites that bind to one and two interfacial Ni atoms, respectively. Furthermore, one surface oxygen site on ZnO(000$\bar{1}$) near the Ni_{nr}/ZnO interface was considered, referred to as the *s* site.

3. Results and discussion

3.1. Adsorption properties of sulfur

The adsorption structures of S on supported/unsupported Ni nanorods are presented in Fig. 2. The adsorption energies (ΔE_{ads}) and geometric parameters are listed in Table 1. Corresponding to the interfacial and surface oxygen sites in the Ni_{nr}/ZnO model, two interfacial O_v sites, $O_v(i1)$ and $O_v(i2)$, and one surface O_v site, $O_v(s)$, were considered, respectively. For S adsorption on unsupported Ni_{nr} (Fig. 2(a)–(e)), the S atom was stably located at the hollow sites of the top and front facets, named as S@*t* and S@*h*1–*h*4 sites, respectively. The *t* site of the Ni nanorod contained more coordination-unsaturated Ni atoms, which accounted for its more negative ΔE_{ads} of −5.44 eV, comparable with the ΔE_{ads} of approximately −5.53 eV for S adsorption on Ni_{55} cluster (Zhu et al., 2021). The *h*1–*h*4 sites on the front (111) facet with ΔE_{ads} of approximately −5.23 eV are closer to the terrace sites on the Ni(111) surface which involves an ΔE_{ads} of around −5.30 eV for S adsorption (Zhu et al., 2021). On the supported Ni nanorods with and without interfacial O_v, the adsorption structures and energies of S are similar to the cases of unsupported Ni_{nr} (Fig. 2(f)–(j)). The S–Ni bond lengths and ΔE_{ads} varied slightly, no more than 0.04 Å and 0.1 eV (Table 1), respectively. Thus, the ZnO substrate and Ni/ZnO interfacial O_v have small influence on the S adsorption over Ni_{nr}. In addition, the ΔE_{ads} of S adsorption follows the order of $t < h1 < h2 < h3 < h4$, indicating that S atoms preferentially adsorb along the top-edge of Ni_{nr}. Hammer and Nørskov (2000) suggested that the binding energy of adsorbates on metal substrate correlates with the d-band center (ε_d). The closer the ε_d is located to the Fermi level, the stronger the binding strength between the metal atoms and adsorbates would be, and vice versa. As shown in Fig. 2(k), the calculated ε_d of different Ni sites locate at −1.057 (*t*), −1.123 (*h*1), −1.178 (*h*2), −1.180 (*h*3), and −1.251 (*h*4) eV, respectively. A linear correlation was found between ΔE_{ads} and ε_d (Fig. 2(l)), which explains the ΔE_{ads} order of S adsorption on Ni_{nr}.

When moving the S atom from Ni_{nr} to the interfacial region and ZnO surface, S adsorption becomes unstable if no O_v is involved and migrates back to Ni_{nr} (*h*4 site) after optimization. Along the rim of Ni_{nr}/ZnO interface, S could only adsorb at the interfacial $O_v(i1)$ and $O_v(i2)$ sites, as shown in Fig. 3(a) and (b). The ΔE_{ads} of S@$O_v(i1)$ and S@$O_v(i2)$ were −5.10 and −5.23 eV, respectively. Despite the difference in the coordination environment between the interfacial O(*i*1) and O(*i*2) atoms, the adsorption configurations and energies of S at the $O_v(i1)$ and $O_v(i2)$ sites were very close. The S@$O_v(i1)$ and S@$O_v(i2)$ involved the same five-coordination structure, bonding to nearest-neighbour three Zn and two Ni atoms simultaneously. The geometric differences between S@$O_v(i1)$ and S@$O_v(i2)$ were small, mirrored by the slight variations of the S–Ni and S–Zn bond lengths (<0.05 Å, Table S1 in ESM); the difference in the total energy between the two model systems was only 0.07 eV. The reason why S@$O_v(i1)$ and S@$O_v(i2)$ changed from "the difference" to "the same" lies in a larger covalent radius of S atom (1.04 Å) compared with that of O atom (0.74 Å). When filling into interfacial O_v, the larger S atom was easier to bond with the bottom-edge Ni atoms along the rim of Ni/ZnO interface and tended to form a more stable interfacial structure with more S–Ni bonds. In S@$O_v(i2)$, the S atom acted like the O(*i*2) atom, forming the maximum two S–Ni bonds. In S@$O_v(i1)$, the S atom at first bonded to one Ni atom like the O(*i*1) atom. However, this original configuration for S@$O_v(i1)$ was not stable and then reconstructed towards a lower-energy structure. The reconstruction process of the initial S@$O_v(i1)$ involved a slight shift of Ni nanorod along the rim of Ni/ZnO interface, leading to the formation of two S–Ni bonds as well as the same structure with S@$O_v(i2)$. Therefore, the adsorption structures and energies of S at Ni_{nr}/ZnO interfacial O_v were less affected by the type of interfacial O_v. For simplicity, $O_v(i1)$ was chosen as the representative of interfacial O_v to investigate the interfacial sulfur transfer pathway. In addition, the S adsorption at the $O_v(s)$ site was calculated (Fig. 3(c)). Due to the absence of the S–Ni interaction, the bonding strength of S@$O_v(s)$ became weak, with an ΔE_{ads} of −3.79 eV.

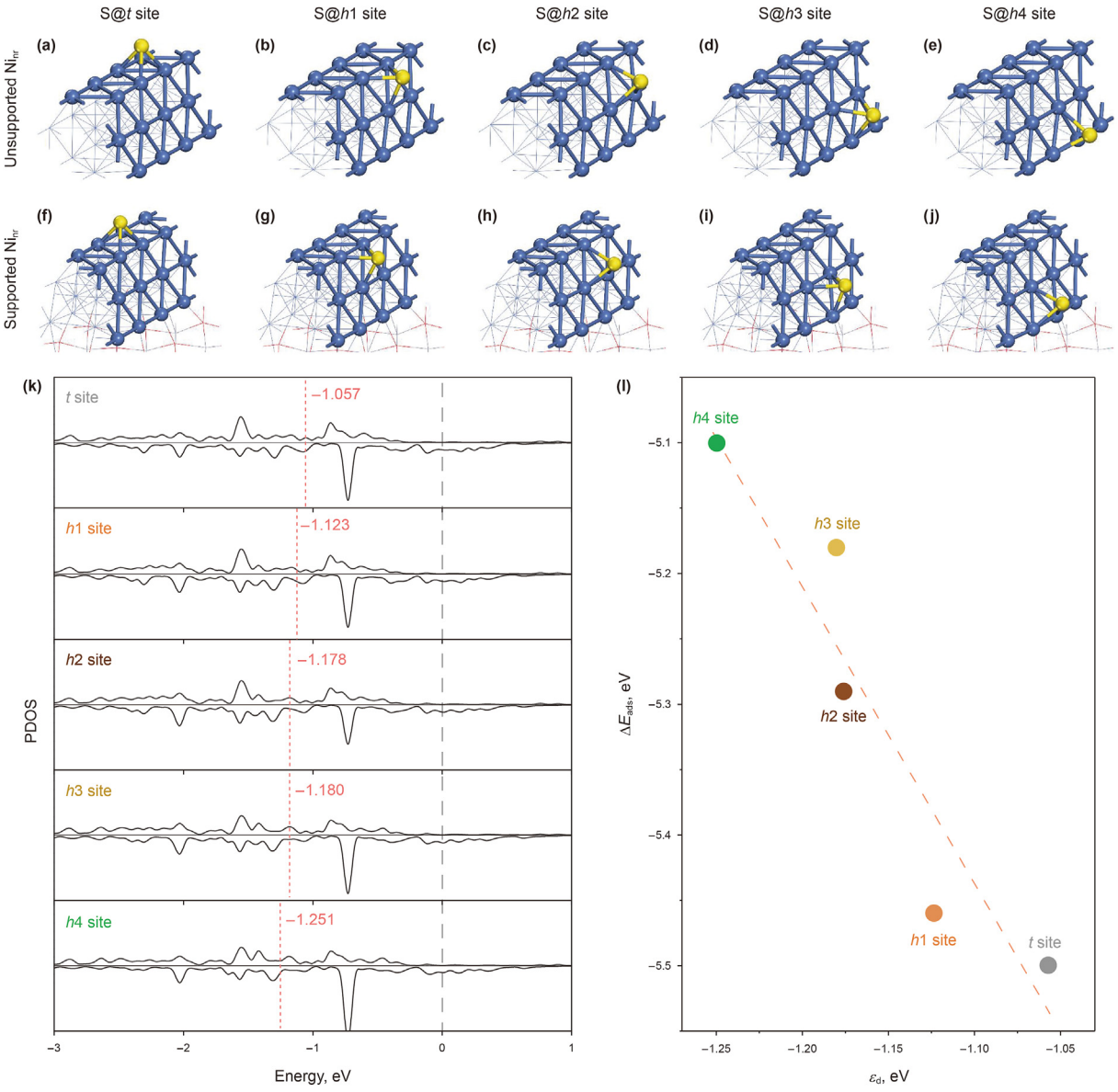

Fig. 2. Optimized adsorption structures of sulfur on unsupported (**a**–**e**) and supported (**f**–**j**) Ni sites. The S atom is shown in yellow color. (k) Projected density of states (PDOS) on different Ni sites. The location of the d-band center (ε_d) is labeled in each case. (l) Illustration of the linear correlation between ΔE_{ads} and ε_d. The equation of linear regression is $\Delta E_{ads} = -2.270 \cdot \varepsilon_d - 7.933$ (eV); the square of the correlation coefficient R^2 (0.889) and the standard error σ (0.066 eV) suggest that the linear relation roughly holds.

Table 1
Binding sites, geometric parameters (Å) and adsorption energies (ΔE_{ads}*, eV) for S atom on supported/unsupported Ni nanorod models.

Models		Properties	Sites				
			t	*h*1	*h*2	*h*3	*h*4
Unsupported Ni nanorod		d_{S-Ni}	2.165/2.163/2.158	2.168/2.134/2.134	2.129/2.157/2.157	2.152/2.121/2.153	2.094/2.130 /2.127
		ΔE_{ads}	−5.44	−5.39	−5.25	−5.18	−5.10
Supported Ni nanorod	w/o O_v	d_{S-Ni}	2.162/2.145/2.146	2.162/2.131/2.130	2.134/2.152/2.157	2.143/2.132/2.138	2.095/2.159 /2.160
		ΔE_{ads}	−5.50	−5.46	−5.29	−5.18	−5.02
	With O_v(*i*1)	d_{S-Ni}	2.158/2.156/2.151	2.166/2.135/2.128	2.125/2.166/2.158	2.155/2.138/2.146	2.108/2.165 /2.144
		ΔE_{ads}	−5.47	−5.45	−5.35	−5.20	−5.09
	With O_v(*i*2)	d_{S-Ni}	2.157/2.146/2.146	2.159/2.131/2.131	2.135/2.157/2.154	2.148/2.133/2.134	2.093/2.160 /2.162
		ΔE_{ads}	−5.52	−5.45	−5.27	−5.19	−5.01

* Adsorption energy could be defined as $\Delta E_{ads} = E_{S/Ni} - E_S - E_{Ni}$. E_S and E_{Ni} are the energies of free S atom in gas phase and Ni substrate, respectively. $E_{S/Ni}$ is the total energy of the S@Ni$_{nr}$ system. Therefore, the negative value of ΔE_{ads} corresponds to stable adsorption.

3.2. Reaction pathways of sulfur transfer

3.2.1. Initial hydrogenation and surface diffusion of S on Ni nanorod

As shown in Fig. 4(a), the initial hydrogenations of S (S + H → SH) at *h*1–*h*4 sites on Ni_{nr} were investigated, and the energy barriers were 1.01, 0.91, 0.86, and 0.82 eV, respectively. The SH group was not stable at the *t* site of the top facet and dissociated back into atomic S and H spontaneously. Owing to the higher energy barrier for S hydrogenation at the *h*1 site, the formation of SH was relatively difficult near the top-edge of Ni_{nr}, which involves more low-coordinated Ni atoms. S diffusion on Ni_{nr} included the movements crossing-over the ridge (top-edge) between the top and front facets (S@*t* ↔ S@*h*1) and those within the front (111) facet (S@*h*1 ↔ S@*h*2 ↔ S@*h*3 ↔ S@*h*4), as shown in Fig. 4(b). The former and the latter contained the average energy barriers of 0.51 and 0.18 eV, respectively. Higher energy barrier involved in crossing-over the top-edge of Ni_{nr} indicates a hindered diffusion for S moving from the (111) front-facet to the top-facet or vice versa. Thus, the deposited S on the top-facet of Ni_{nr} was more stable than that on the (111) front-facet because the hydrogenation and diffusion processes of S were blocked on the top-facet. Taking the *t* site on the top-facet of Ni_{nr} to represent low-coordinated sites of Ni nanoparticles, the low-coordinated Ni site, such as corner and edge, could be deduced as more liable to form NiS species as the amount of S deposition increases. In addition, the energy barriers of S diffusion were significantly lower than those of initial hydrogenation, indicating that S diffusion is preferred to its hydrogenation on Ni_{nr}, consistent with the previous DFT results on Ni(111) and Ni_{55} (Zhu et al., 2021). Experiments performed by Bezverkhyy et al. (2008) on Ni/ZnO catalysts also suggested that a surface sulfur layer forms rapidly on Ni after Ni/ZnO having contact with the mixture of H_2 and thiophene. Thus, direct S diffusion is preferred on Ni_{nr} compared with the hydrogenation of S.

3.2.2. S transfer at Ni_{nr}/ZnO interface

The PES of S transfer at the Ni_{nr}/ZnO interface is displayed in Fig. 5 with the corresponding schematic structures involved. The transfer process includes the direct S migration from S@*h*4 into the interfacial O_v, denoted as the interfacial S transfer pathway (Path I), and the hydrogenation of S towards H_2S, denoted as the H_2S transfer pathway (Path II). The possibility of SH intermediate moving into the interfacial O_v was also considered (Path III). S@*h*4 was chosen as the starting point for S transfer because compared with other sites, the *h*4 site involved the lowest $|\Delta E_{ads}|$ and the corresponding weakest binding strength for S adsorption on Ni_{nr}, which is most beneficial for the initial hydrogenation of S (Fig. 4(a)) and final formation of H_2S. Path I involved the energy barrier of 0.47 eV for the direct S transfer from S@*h*4 into O_v(*i*1). For comparison, the S diffusion towards O_v(*i*1) starting from the *h*3 site (Fig. S2 in ESM) involved a higher energy barrier of 0.57 eV, indicating that the direct S transfer from S@*h*3 into O_v(*i*1) is unfavorable. In Path II, the IS was the co-adsorbed S@*h*4 and H atoms. The two-step hydrogenation barriers of S + 2H → SH + H → H_2S were calculated to be 1.04 and 1.21 eV, respectively. However, the inverse process of Path II involved much lower energy barriers for H_2S → SH + H (0.34 eV) and SH → S + H (0.12 eV), implying that the H_2S dissociation to S is more favorable than the S hydrogenation to H_2S on Ni. The ΔE_{ads} for H_2S was calculated to be −0.69 eV. The desorption process of H_2S from Ni_{nr} into gas phase could cost at least 0.69 eV, higher than the energy barrier for the S–H bond cleavages of H_2S (0.34 eV). This result further confirmed that the adsorbed H_2S on Ni is unstable and tends to dissociate rather than desorb from Ni. Path III started with the intermediate state of Path II, SH@*h*4, and ended with SH@O_v(*i*1). This SH transfer step costs a relatively low energy barrier of 0.35 eV. In addition, possibilities of S/SH transfer towards the surface O_v of ZnO (O_v(*s*)), which are adjacent to the Ni_{nr}/ZnO interfacial region, were explored. The energy barrier for S migration from Ni_{nr} to the O_v(*s*) site increased significantly to 1.79 eV, whereas the energy barrier for SH transfer remained as low as 0.48 eV (Fig. S3 in ESM). Although the SH group showed a stronger diffusibility than S atom, mirrored by lower diffusion barriers (~0.42 eV) when crossing over the Ni/ZnO interfacial region, the initial hydrogenation step to form the SH group involved relatively high energy barriers (~0.93 eV). Meanwhile, the SH dissociation back to S was easy to occur with even lower barriers (~0.12 eV), indicating the inhibition of SH diffusion process for S transfer. To sum up, hydrogenation of S to SH/H_2S on Ni_{nr} and subsequent H_2S desorption are very difficult compared with the direct S transfer from Ni_{nr} to the interfacial O_v. Thus, the interfacial S transfer (Path I) could be identified as a feasible reaction pathway in the RADS mechanism rather than the classic S transfer via H_2S (Path II) and the SH diffusion process (Path III). In addition, the Gibbs free energy change (ΔG) for the S transfer process was further calculated, and the ΔG diagram is displayed in Fig. S4 of the ESM with the corresponding schematic structures. Path I involved the lowest ΔG (0.041 eV) compared with Paths II and III. This finding indicated the thermodynamic favorability of Path I over Paths II and III, consistent with the above kinetic results.

3.3. Role of H_2 in the formation of O_v and H_2O

3.3.1. Thermodynamic analysis for surface O_v formation on ZnO(000$\bar{1}$)

Experimentally, Ni/ZnO catalysts are prepared through

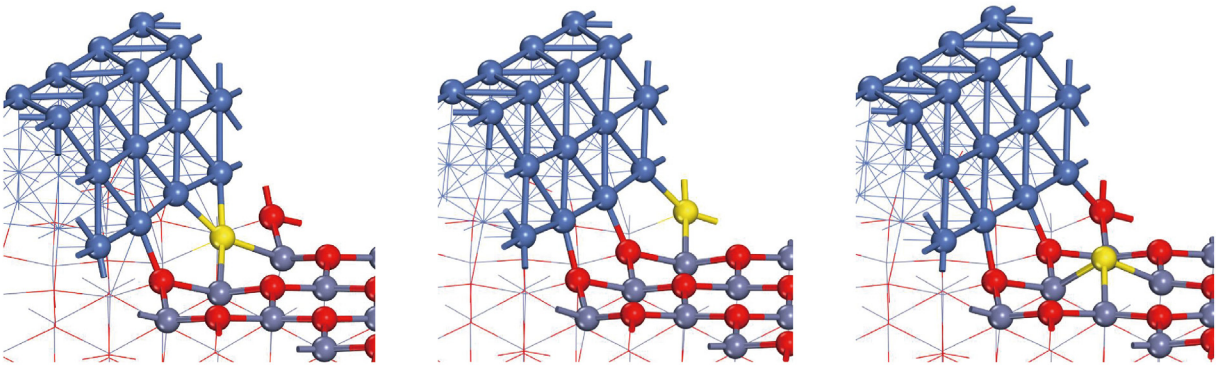

(a) S@O_v(*i*1) site **(b)** S@O_v(*i*2) site **(c)** S@O_v(*s*) site

Fig. 3. S adsorption at the interfacial O_v(*i*1) site (**a**), interfacial O_v(*i*2) site (**b**), and surface O_v(*s*) site (**c**).

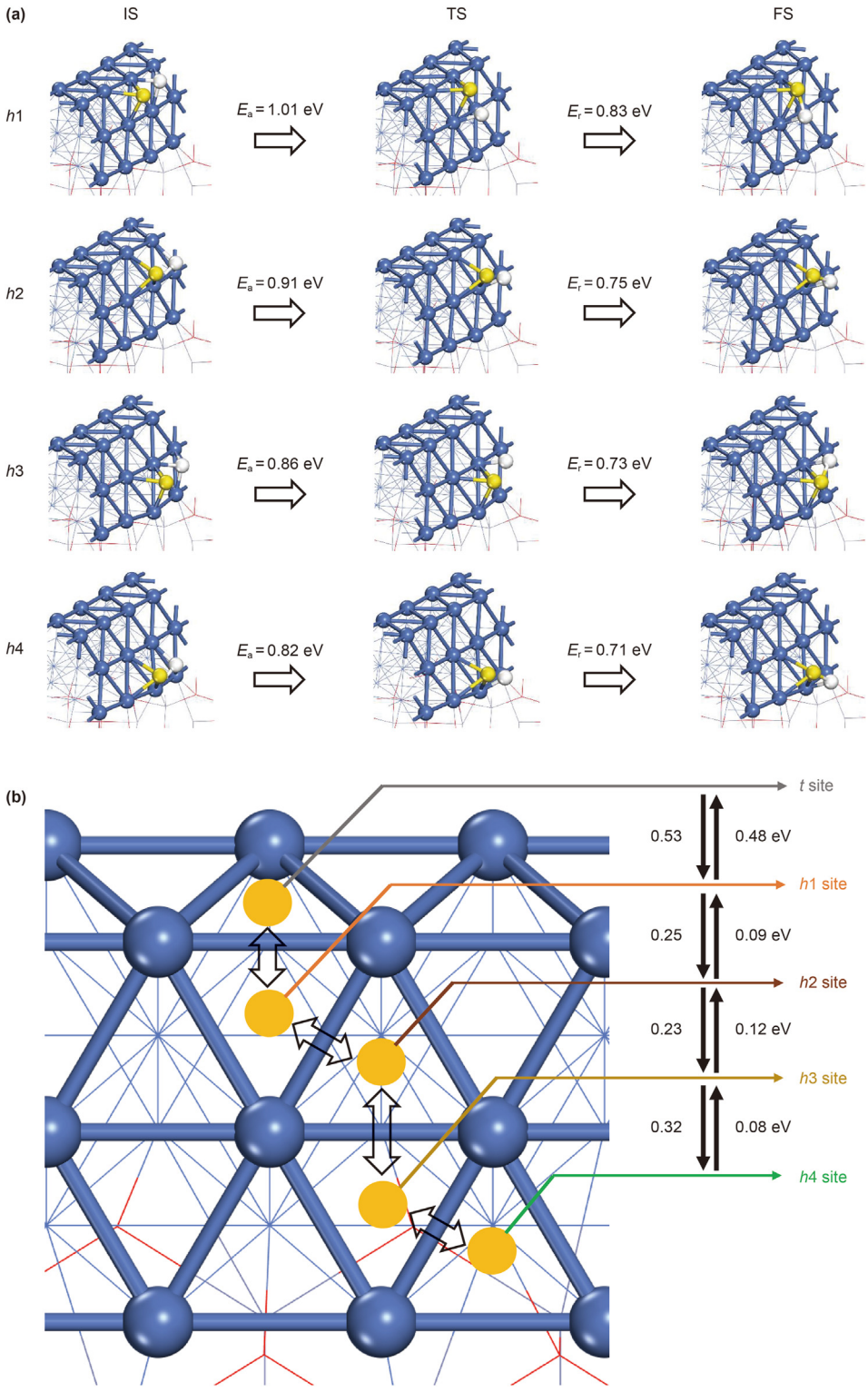

Fig. 4. (**a**) Initial hydrogenation pathways of S at *h*1–*h*4 sites on Ni_{nr}. The energy reference is set as the total energy of S@*h*-site plus two atomic H adsorbed at infinitely separated *h* sites on Ni_{nr}. The adsorbed H atom is omitted for simplicity. (**b**) S diffusion of S@*t* ↔ S@*h*1 ↔ S@*h*2 ↔ S@*h*3 ↔ S@*h*4 on Ni_{nr}. The energy barriers (eV) of each step and its reverse process are given.

impregnation or co-precipitation methods, followed by calcination (or annealing) treatment in air and hydrogen reduction (Ryzhikov et al., 2008; Ullah et al., 2017; Zhang et al., 2013). Given the existence of interfacial O_v is an essential prerequisite for S diffusion from Ni_{nr} to ZnO substrate, it is necessary to examine the presence status of surface O_v on ZnO during the preparation process, such as calcination (O_2 atmosphere) and reduction (H_2 atmosphere) steps. Ab initio thermodynamics analysis was performed on ZnO($000\bar{1}$) to identify stable O_v-containing surfaces as a function of O_2/H_2 partial pressure and temperature. In accordance with previous

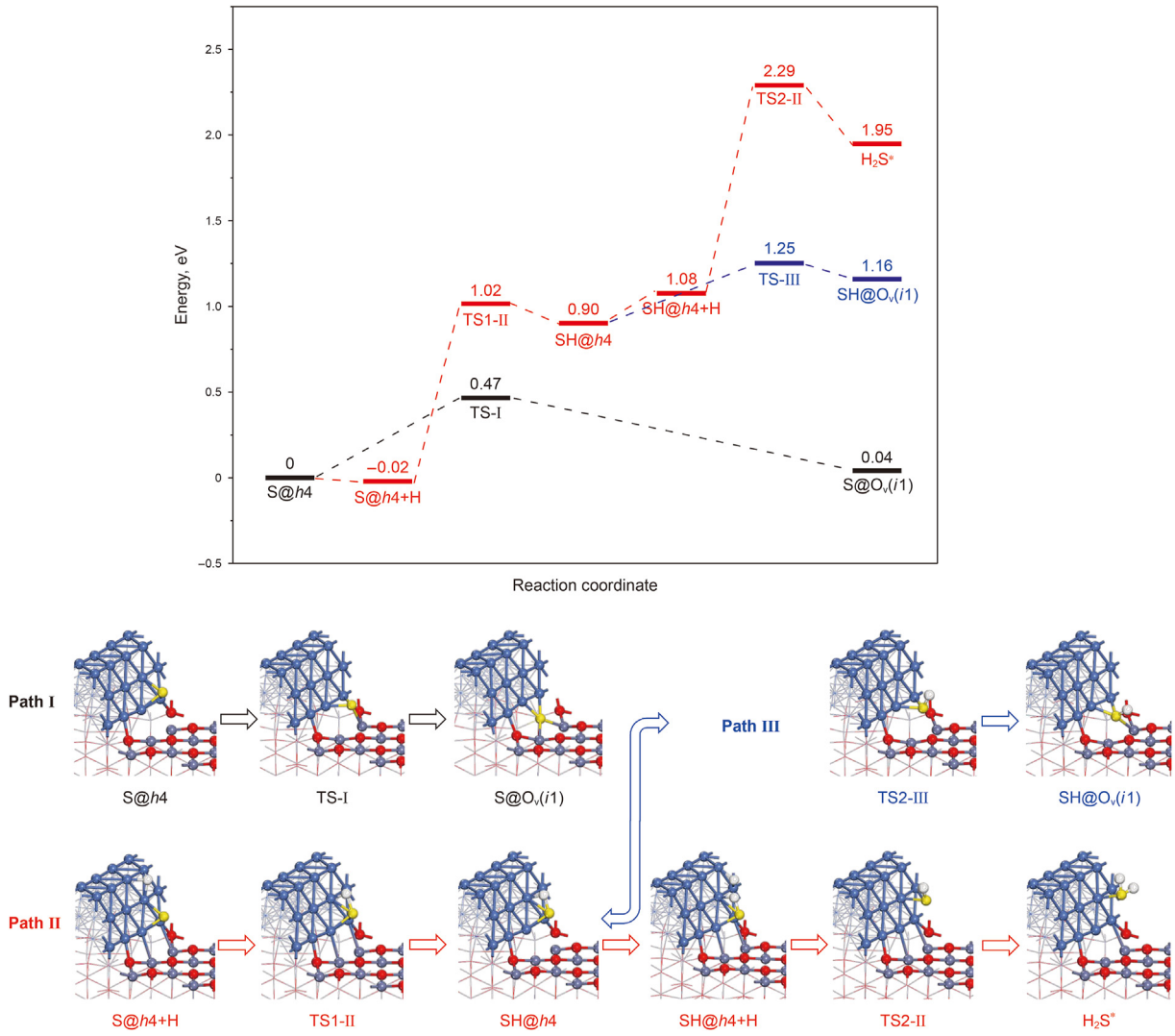

Fig. 5. S transfer pathways (Paths I–III) at the Ni_{nr}/ZnO interface. Paths I–III are labeled black, red, and blue colors, respectively. The energy reference is set as the total energy of the S@*h*4 configuration plus two adsorbed H atoms at infinitely separated sites on Ni_{nr}. The adsorbed H atom is omitted for simplicity.

experimental works, the preparation condition for calcination was set as $P_{O_2} = 1$ atm and $T = 673.15$ K (Tang et al., 2015; Zhang et al., 2010), and the preparation condition for reduction was set as $P_{H_2} = 10$ atm and $T = 673.15$ K (Meng et al., 2013; Song et al. 2021). For simplicity, a ZnO($000\bar{1}$) slab with a 3 × 3 surface supercell was used, which included nine surface oxygen atoms. One surface O_v represents 1/9 (11.11%) O_v concentration. When taking into account four surface O_v, significant deformations of surface structure were observed, indicating that the generation of four surface O_v is thermodynamically infeasible. Thus, three surface O_v were considered at most on ZnO($000\bar{1}$). Accordingly, three types of surface O_v-containing structures were built (Fig. S5 in ESM): Type I with one O_v, Type II with two O_v, and Type III with three O_v. All possible structures were optimized, and the most stable ones were chosen to represent the O_v-containing surface for each type.

A surface phase diagram of ZnO($000\bar{1}$) under O_2 atmosphere was plotted by calculating the free energy changes in surface O_v formation ($ZnO \rightarrow ZnO_{nO_v} + \frac{n}{2}O_2$) as a function of O_2 partial pressure and temperature:

$$\Delta G = E_{surf\_nO_v} + \frac{n}{2}G_{O_2} - E_{surf} \quad (2)$$

where n is the number of O_v ($n = 1$–3); $E_{surf\_nO_v}$ and E_{surf} are the energies of ZnO slab with and without nO_v, respectively; and G_{O_2} is the free energy contribution of O_2 represented by the chemical potential of $\mu_{O_2}(T, P)$. Similarly, a surface phase diagram of ZnO($000\bar{1}$) under H_2 atmosphere was plotted by calculating the free energy changes in surface O_v formation ($ZnO + nH_2 \rightarrow ZnO_{nO_v} + nH_2O$) as a function of temperature and partial pressures of H_2O and H_2:

$$\Delta G = E_{surf\_nO_v} + nG_{H_2O} - E_{surf} - nG_{H_2} \quad (3)$$

where G_{H_2O} and G_{H_2} are the free energy contributions of H_2O and H_2 represented by the chemical potentials of $\mu_{H_2O}(T, P)$ and $\mu_{H_2}(T, P)$, respectively.

$$\mu_X(T,P)=\mu_X(T,P^\Theta)+RT\ln\left(\frac{P}{P^\Theta}\right)=\left[H_\cdot(X)(T,P^\Theta)-H_X(0K,P^\Theta)\right]-T\bullet S_X(T,P^\Theta)+RT\ln\left(\frac{P}{P^\Theta}\right) \quad (4)$$

where the X denotes gas-phase O_2, H_2O and H_2. The enthalpy $H_X(T,P^\Theta)$ and entropy $S_X(T,P^\Theta)$ of gas-phase molecule could be obtained from the NIST Standard Thermodynamic Tables (NIST Chemistry WebBook). The resulting phase diagrams in Fig. 6 indicated that the ZnO(000$\bar{1}$) surface contained only one O_v in the calcination condition ($P_{O_2}=1$ atm, $T=673.15$ K) but involved three O_v in the reduction condition ($P_{H_2}=10$ atm, $T=673.15$ K). The surface O_v concentration (33.3%) of ZnO(000$\bar{1}$) in the H_2 atmosphere was three times higher than that (11.1%) in the O_2 atmosphere, demonstrating that the hydrogen reduction step in the preparation of Ni/ZnO samples facilitated the formation of O_v on ZnO. For freshly prepared catalysts, it's reasonable to infer that a significant amount of O_v already existed along the rim of Ni/ZnO interface, which are pivotal for the following interfacial sulfur diffusion.

3.3.2. Reaction pathway for the formation of interfacial O_v and H_2O

In addition to those interfacial O_v that already existed in the Ni/ZnO system after the catalyst preparation, the subsequent RADS under H_2 atmosphere could produce O_v at the interface region. The calculated PES for the formation of interfacial O_v and H_2O is displayed in Fig. 7 with the corresponding schematic structures involved. This process (Path IV) mainly included three reaction steps: (1) first hydrogenation of the interfacial O atom, forming an interfacial O–H group; (2) diffusion of the O–H group from Ni_{nr}/ZnO interface to Ni_{nr}, leaving behind an interfacial O_v; (3) secondary hydrogenation of the O–H group, yielding adsorbed H_2O* on Ni_{nr}. The Ni_{nr}/ZnO model without O_v was taken as the starting point of the reactions. The first hydrogenation step began from the H@$h4$ site with the H addition to the interfacial O($i1$) atom. In the TS1-IV, the H atom has moved to the Ni–Ni bridge site at the bottom-edge of Ni_{nr}; one Ni–H bond length increased to 3.058 Å from its original 1.661 Å indicating of the cleavage of this Ni–H bond, whereas the other two Ni–H bond lengths (1.631/1.711 Å) decreased slightly compared with their original values (1.676/1.745 Å) in the H@$h4$ configuration. The energy barrier and reaction energy of this step were 1.05 and 0.40 eV, respectively. In the FS (OH@O_v($i1$)), the newly formed O($i1$)–H bond length was 0.992 Å. The formation of the O($i1$)–H group led to a considerable increase in the average bond length of three Zn–O($i1$) bonds, from original 2.015 to 2.416 Å. This result indicated that the bond strength between the interfacial O($i1$) atom and ZnO substrate was weakened because of the hydrogenation to O($i1$). Then, the O($i1$)–H group migrated back to the $h4$ site on Ni_{nr} with a relatively low barrier of 0.58 eV, leaving behind an oxygen vacancy, O_v($i1$), at the Ni_{nr}/ZnO interface. The secondary hydrogenation started with the co-adsorption configuration of the OH group and atomic H on adjacent $h4$ sites, followed by the addition of H to OH and the subsequent formation of adsorbed H_2O*. This step involved an energy barrier of 1.06 eV without endo- or exothermicity. H_2O bound to Ni_{nr} through a single O–Ni bond, and the O–Ni bond length was 2.151 Å, larger than the sum of covalent radius for O and Ni atoms (1.99 Å). This result indicated that the binding of H_2O to Ni_{nr} was weak, in accordance with its relatively lower ΔE_{ads} of −0.47 eV H_2O desorption from Ni_{nr} into gas phase could cost 0.47 eV, much lower than the energy barrier for the O–H bond cleavage of H_2O* (1.06 eV), implying that the adsorbed H_2O* tended to desorb rapidly once formed rather than dissociate.

For comparison, the direct diffusion path (Path V, Fig. 7) of interfacial O($i1$) upwards to Ni_{nr} was also calculated, commonly referred to as the reverse spillover of lattice oxygen atoms (Davó-Quiñonero et al., 2020; Parastaev et al., 2020; Su et al., 2021; Vayssilov et al., 2011; Zhang et al., 2016). This process needed to overcome an energy barrier of 1.33 eV, much higher than the energy barrier of 0.58 eV for the upward movement of the O($i1$)–H group. Through comparison of relevant energy barriers, the stepwise hydrogenation of interfacial O followed by H_2O desorption (Path IV) was found to be more favorable than the direct diffusion path of interfacial O upwards to Ni nanorod (Path V). To sum up, hydrogenation to interfacial O($i1$) could facilitate the reverse spillover of interfacial oxygen atoms from ZnO substrate to Ni_{nr}, leading to interfacial O_v genaration and subsequent H_2O desorption from Ni_{nr}. The average energy barrier of 1.06 eV for stepwise hydrogenation could be overcome at the reaction temperature of

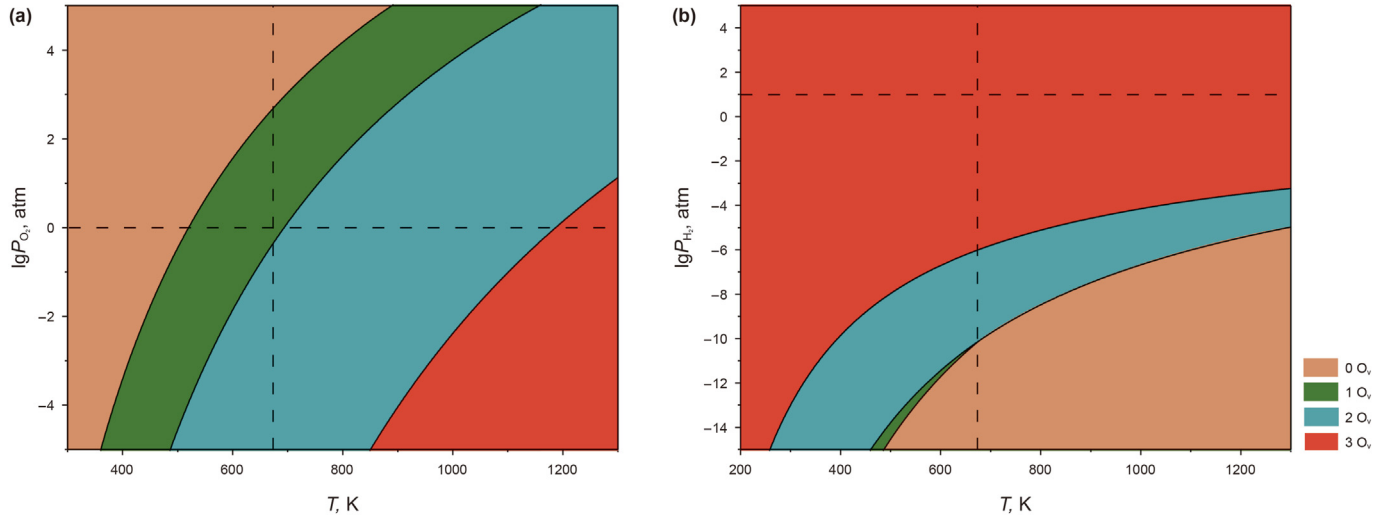

Fig. 6. Calculated phase diagrams for ZnO surface under O_2 (**a**) and H_2 (**b**) atmospheres. Different colored areas represent four thermodynamically stable structures for given temperatures and gas partial pressures. The surfaces with zero, one, two, and three surface O_v are colored with light orange, green, blue, and red, respectively. The dashed lines represent the calcination condition ($P_{O_2}=1$ atm, $T=673.15$ K) and the reduction condition ($P_{H_2}=10$ atm, $T=673.15$ K) for Ni/ZnO catalysts.

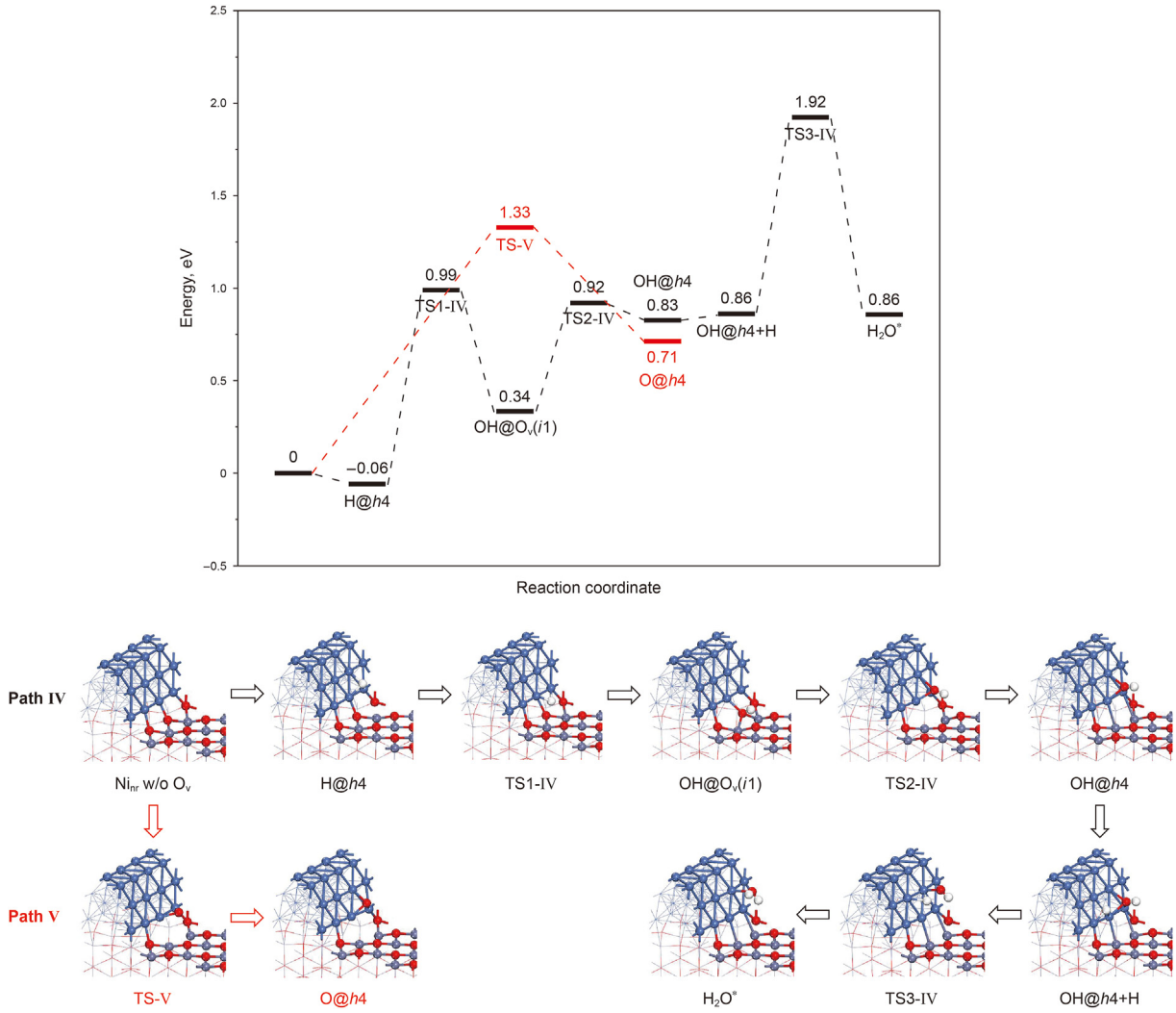

Fig. 7. Reaction pathways of interfacial O_v formation at the Ni_{nr}/ZnO interface. Path IV and V are labeled black and red colors, respectively. The energy reference is set as the total energy of the O_v-free Ni_{nr}/ZnO model plus two adsorbed H atom at infinitely separated sites on Ni_{nr}. The adsorbed H atom is omitted for simplicity.

700 K on the basis of the estimation from the Arrhenius equation, demonstrating that under RADS condition, interfacial O_v of Ni/ZnO could also be produced and then promote the interfacial S transfer from Ni_{nr} to ZnO substrate. In addition, the ΔG of Paths IV and V was further calculated, and the results were presented in Fig. S6 of ESM. Path V involved higher ΔG value (0.609 eV) than Path IV, which indicated the thermodynamic favorability of Path IV over Path V, in agreement with the above kinetic results.

4. Conclusions

DFT calculations were performed to study the sulfur transfer mechanism of reactive adsorption desulfurization on Ni/ZnO catalysts. S atoms preferentially adsorbed on the low-coordinated Ni sites, where the hydrogenation and diffusion processes of S were blocked. S diffusion has priority over its hydrogenation on Ni, in good agreement with the previous theoretical and experimental results. At the Ni/ZnO interface, stable S adsorption could only occur at interfacial O_v sites. Hydrogenation of S to SH/H_2S on Ni and subsequent H_2S desorption were much more difficult than the direct S transfer from Ni to the interfacial O_v. The interfacial S transfer could thus be identified as a feasible reaction pathway in the RADS mechanism rather than the classic S transfer via H_2S and the SH diffusion process, and the existence of interfacial O_v is an essential prerequisite for this solid-state diffusion. The ab initio thermodynamics analysis showed that the hydrogen reduction step in the preparation of Ni/ZnO samples could promote the formation of surface O_v on ZnO, which accounts for the presence of interfacial O_v in freshly prepared catalysts. The calculations also demonstrated that hydrogenation of interfacial O atoms to form O–H group could facilitate the reverse spillover of these lattice O atoms from ZnO to Ni, accompanied with the interfacial O_v generation. In addition, H_2O was produced by further hydrogenation and desorbed from Ni rather than ZnO. The ZnO surface provides O_v to accommodate S atoms transferred from Ni, and H_2 plays a key role in facilitating the O_v formation. This work provides a deep understanding of the RADS process within the Ni/ZnO catalyst system and shows the importance of Ni/ZnO interface on the RADS mechanism, shedding light on the design of more active metal/oxide catalysts towards catalytic desulfurization.

Declaration of competing interest

The authors declare that they have no known competing financial interests or personal relationships that could have appeared to influence the work reported in this paper.

Acknowledgments

This work was supported by the National Natural Science Foundation of China (22178388, 21776315), the Taishan Scholars Program of Shandong Province (tsqn201909065), and the Fundamental Research Funds for the Central Universities (19CX05001A).

Appendix A. Supplementary data

Supplementary data to this article can be found online at https://doi.org/10.1016/j.petsci.2023.05.014.

References

Babich, I., Moulijn, J., 2003. Science and technology of novel processes for deep desulfurization of oil refinery streams:a review. Fuel 82 (6), 607–631. https://doi.org/10.1016/S0016-2361(02)00324-1.

Bezverkhyy, I., Ryzhikov, A., Gadacz, G., et al., 2008. Kinetics of thiophene reactive adsorption on Ni/SiO_2 and Ni/ZnO. Catal. Today 130 (1), 199–205. https://doi.org/10.1016/j.cattod.2007.06.038.

Blöchl, P.E., 1994. Projector augmented-wave method. Phys. Rev. B 50 (24), 17953–17979. https://doi.org/10.1103/PhysRevB.50.17953.

Davó-Quiñonero, A., Bailón-García, E., López-Rodríguez, S., et al., 2020. Insights into the oxygen vacancy filling mechanism in CuO/CeO_2 catalysts: a key step toward high selectivity in preferential CO oxidation. ACS Catal. 10 (11), 6532–6545. https://doi.org/10.1021/acscatal.0c00648.

Duan, M., Yu, J., Meng, J., et al., 2018. Reconstruction of supported metal nanoparticles in reaction conditions. Angew. Chem. 130 (22), 6574–6579. https://doi.org/10.1002/anie.201800925.

Gislason, J., 2001. Phillips sulfur-removal process nears commercialization. Oil Gas J. 99 (47), 72.

Green, I.X., Tang, W., Neurock, M., et al., 2011. Spectroscopic observation of dual catalytic sites during oxidation of CO on a Au/TiO_2. Science 333 (6043), 736–739. https://doi.org/10.1126/science.1207272.

Gupta, M., He, J., Nguyen, T., et al., 2016. Nanowire catalysts for ultra-deep hydrodesulfurization and aromatic hydrogenation. Appl. Catal. B Environ. 180, 246–254. https://doi.org/10.1016/j.apcatb.2015.06.029.

Hammer, B., Nørskov, J.K., 2000. Theoretical surface science and catalysis–calculations and concepts. Adv. Catal. 45, 71–129. https://doi.org/10.1016/S0360-0564(02)45013-4.

Henkelman, G., Jónsson, H., 1999. A dimer method for finding saddle points on high dimensional potential surfaces using only first derivatives. J. Chem. Phys. 111 (15), 7010–7022. https://doi.org/10.1063/1.480097.

Henkelman, G., Uberuaga, B.P., Jónsson, H., 2000. A climbing image nudged elastic band method for finding saddle points and minimum energy paths. J. Chem. Phys. 113 (22), 9901–9904. https://doi.org/10.1063/1.1329672.

Huang, H., Salissou, M., Yi, D., et al., 2013. Study on reactive adsorption desulfurization of model gasoline on Ni/ZnO-HY adsorbent. China Pet. Process. Petrochem. Technol. 3, 57–64.

Huang, L., Wang, G., Qin, Z., et al., 2010. A sulfur K-edge XANES study on the transfer of sulfur species in the reactive adsorption desulfurization of diesel oil over Ni/ZnO. Catal. Commun. 11 (7), 592–596. https://doi.org/10.1016/j.catcom.2010.01.001.

Huang, L., Wang, G., Qin, Z., et al., 2011. In situ XAS study on the mechanism of reactive adsorption desulfurization of oil product over Ni/ZnO. Appl. Catal. B Environ. 106 (1–2), 26–38. https://doi.org/10.1016/j.apcatb.2011.05.001.

Ji, J., Zhao, L., Gao, J., 2012. DFT study on the sequential desulfurization mechanism of reactive adsorption desulfurization [Online]. Chinese Sciencepaper Online. http://www.paper.edu.cn/releasepaper/content/201212-963 (in Chinese).

Jiang, W., Xiao, J., Gao, X., et al., 2021. In situ fabrication of hollow silica confined defective molybdenum oxide for enhanced catalytic oxidative desulfurization of diesel fuels. Fuel 305, 121470–121480. https://doi.org/10.1016/j.fuel.2021.121470.

Johnson III, R.D., 2015. NIST Computational Chemistry Comparison and Benchmark Database, NIST Standard Reference Database Number 101, Release 18. October 2016. https://cccbdbnistgov.

Kang, X., Liu, J., Tian, C., et al., 2020. Surface curvature-confined strategy to ultrasmall nickel-molybdenum sulfide nanoflakes for highly efficient deep hydrodesulfurization. Nano Res. 13 (3), 882–890. https://doi.org/10.1007/s12274-020-2716-x.

Karzel, H., Potzel, W., Köfferlein, M., et al., 1996. Lattice dynamics and hyperfine interactions in ZnO and ZnSe at high external pressures. Phys. Rev. B 53 (17), 11425–11438. https://doi.org/10.1103/PhysRevB.53.11425.

Khare, G.P., 2001. Desulfurization Process and Novel Bimetallic Sorbent Systems for Same. U.S. Patent, 6274533.

Khare, G.P., 2004. Engelbert, D.R. Desulfurization and Novel Sorbents for Same. U.S.. Patent 6683024.

Kresse, G., Furthmüller, J., 1996a. Efficiency of ab-initio total energy calculations for metals and semiconductors using a plane-wave basis set. Comput. Mater. Sci. 6 (1), 15–50. https://doi.org/10.1016/0927-0256(96)00008-0.

Kresse, G., Furthmüller, J., 1996b. Efficient iterative schemes for ab initio total-energy calculations using a plane-wave basis set. Phys. Rev. B. 54 (16), 11169–11186. https://doi.org/10.1103/PhysRevB.54.11169.

Kresse, G., Joubert, D., 1999. From ultrasoft pseudopotentials to the projector augmented-wave method. Phys. Rev. B. 59 (3), 1758–1775. https://doi.org/10.1103/PhysRevB.59.1758.

Kumar, S., Chakarvarti, S., 2004. SEM morphology and XRD characterization of Ni microstructure arrays synthesized by dc electrodeposition in porous polycarbonate templates. J. Mater. Sci. 39 (9), 3249–3251. https://doi.org/10.1023/B:JMSC.0000025871.02799.f3.

Li, T., Zhu, H., Yu, Z., et al., 2022. Promotion effects of Ni-doping on H_2S removal and ZnO initial sulfuration over ZnO nanowire by first-principle study. Mol. Catal. 519, 112148–112157. https://doi.org/10.1016/j.mcat.2022.112148.

Ling, L., Zhang, R., Han, P., et al., 2013. DFT study on the sulfurization mechanism during the desulfurization of H_2S on the ZnO desulfurizer. Fuel Process. Technol. 106, 222–230. https://doi.org/10.1016/j.fuproc.2012.08.001.

Liu, J., Liu, X., Yan, R., et al., 2023. Active phase morphology engineering of NiMo/Al_2O_3 through La introduction for boosting hydrodesulfurization of 4,6-DMDBT. Petrol. Sci. 20 (2), 1231–1237. https://doi.org/10.1016/j.petsci.2022.09.023.

Liu, Z., Wang, Y., Li, J., et al., 2014. The effect of γ-Al_2O_3 surface hydroxylation on the stability and nucleation of Ni in Ni/γ-Al_2O_3 catalyst: a theoretical study. RSC Adv. 4 (26), 13280–13292. https://doi.org/10.1039/c3ra46352d.

Mager-Maury, C., Bonnard, G., Chizallet, C., et al., 2011. H_2-induced reconstruction of supported Pt clusters: metal–support interaction versus surface hydride. ChemCatChem 3 (1), 200–207. https://doi.org/10.1002/cctc.201000324.

Meng, X., Huang, H., Shi, L., 2013. Reactive mechanism and regeneration performance of NiZnO/Al_2O_3-diatomite adsorbent by reactive adsorption desulfurization. Ind. Eng. Chem. Res. 52 (18), 6092–6100. https://doi.org/10.1021/ie303514y.

Meng, X., Zhao, Y., Wang, Q., et al., 2014. Deep desulfurization of gasoline: catalysts and technology. Energ. Environ. Focus. 3 (1), 53–59. https://doi.org/10.1166/eef.2014.1092.

NIST Chemistry WebBook. http://webbook.nist.gov/chemistry.

Parastaev, A., Muravev, V., Huertas Osta, E., et al., 2020. Boosting CO_2 hydrogenation via size-dependent metal–support interactions in cobalt/ceria-based catalysts. Nat. Catal. 3 (6), 526–533. https://doi.org/10.1038/s41929-020-0459-4.

Perdew, J.P., Burke, K., Wang, Y., 1996. Generalized gradient approximation for the exchange-correlation hole of a many-electron system. Phys. Rev. B. 54 (23), 16533. https://doi.org/10.1103/PhysRevB.57.14999.

Ryzhikov, A., Bezverkhyy, I., Bellat, J.P., 2008. Reactive adsorption of thiophene on Ni/ZnO: role of hydrogen pretreatment and nature of the rate determining step. Appl. Catal. B Environ. 84 (3–4), 766–772. https://doi.org/10.1016/j.apcatb.2008.06.009.

Silaghi, M.C., Comas-Vives, A., Coperet, C., 2016. CO_2 Activation on Ni/γ–Al_2O_3 catalysts by first-principles calculations: from ideal surfaces to supported nanoparticles. ACS Catal. 6 (7), 4501–4505. https://doi.org/10.1021/acscatal.6b00822.

Song, W., Hensen, E.J.M., 2014. Mechanistic aspects of the water–gas shift reaction on isolated and clustered Au atoms on CeO_2(110). A density functional theory study. ACS Catal. 4 (6), 1885–1892. https://doi.org/10.1021/cs401206e.

Song, Y., Peng, B., Yang, X., et al., 2021. Trail of sulfur during the desulfurization via reactive adsorption on Ni/ZnO. Green Energy Environ 6 (4), 597–606. https://doi.org/10.1016/j.gee.2020.05.010.

Su, Y., Xia, G., Qin, Y., et al., 2021. Lattice oxygen self-spillover on reducible oxide supported metal cluster: the water–gas shift reaction on Cu/CeO_2 catalyst. Chem. Sci. 12 (23), 8260–8267. https://doi.org/10.1039/D1SC01201K.

Suh, I.K., Ohta, H., Waseda, Y., 1988. High-temperature thermal expansion of six metallic elements measured by dilatation method and X-ray diffraction. J. Mater. Sci. 23 (2), 757–760. https://doi.org/10.1007/BF01174717.

Sun, G., Alexandrova, A.N., Sautet, P., 2019. Pt8 cluster on alumina under a pressure of hydrogen: support-dependent reconstruction from first-principles global optimization. J. Chem. Phys. 151 (19), 194703–194711. https://doi.org/10.1063/1.5129296.

Tang, M., Zhou, L., Du, M., et al., 2015. A novel reactive adsorption desulfurization Ni/MnO adsorbent and its hydrodesulfurization ability compared with Ni/ZnO. Catal. Commun. 61, 37–40. https://doi.org/10.1016/j.catcom.2014.11.005.

Tang, M., Wang, W., Zhou, L., et al., 2019. Reactive adsorption desulfurization of thiophene over NiMo/ZnO, a new adsorbent with high desulfurization performance and sulfur capacity at moderate temperature. Catal. Sci. Technol. 9 (22), 6318–6326. https://doi.org/10.1039/C9CY01070J.

Tawara, K., Nishimura, T., Iwanami, H., 2000. Ultra-deep hydrodesulfurization of kerosene for fuel cell system (part 2) regeneration of sulfur-poisoned nickel catalyst in hydrogen and finding of auto-regenerative nickel catalyst. J. Jpn. Petrol. Inst. 43 (2), 114–120. https://doi.org/10.1627/JPI1958.43.114.

Ullah, R., Bai, P., Wu, P., et al., 2017. Superior performance of freeze-dried Ni/ZnO-Al_2O_3 adsorbent in the ultra-deep desulfurization of high sulfur model gasoline. Fuel Process. Technol. 156, 505–514. https://doi.org/10.1016/j.fuproc.2016.10.022.

Vayssilov, G.N., Lykhach, Y., Migani, A., et al., 2011. Support nanostructure boosts oxygen transfer to catalytically active platinum nanoparticles. Nat. Mater. 10 (4), 310–315. https://doi.org/10.1038/nmat2976.

Wang, D., Wang, L., Jiao, Y., et al., 2022. The confined growth of few-layered and ultrashort-slab Ni-promoted MoS_2 on reduced graphene oxide for deep-degree hydrodesulfurization. Nano Res. 15 (8), 7052–7062. https://doi.org/10.1007/s12274-022-4375-6.

Yan, R., Liu, X., Liu, J., et al., 2022. Modulating the active phase structure of NiMo/Al_2O_3 by La modification for ultra-deep hydrodesulfurization of diesel. AIChE J., e17873–e17887 https://doi.org/10.1002/aic.17873.

Zhai, H., Alexandrova, A.N., 2018. Local fluxionality of surface-deposited cluster catalysts: the case of Pt7 on Al_2O_3. J. Phys. Chem. Lett. 9 (7), 1696–1702. https://doi.org/10.1021/acs.jpclett.8b00379.

Zhang, J., Liu, Y., Tian, S., et al., 2010. Reactive adsorption of thiophene on Ni/ZnO adsorbent: effect of ZnO textural structure on the desulfurization activity. J. Nat. Gas Chem. 19 (3), 327–332. https://doi.org/10.1016/S1003-9953(09)60076-1.

Zhang, S., Zhang, Y., Huang, S., et al., 2012. Mechanistic investigations on the adsorption of thiophene over Zn_3NiO_4 bimetallic oxide cluster. Appl. Surf. Sci. 258 (24), 10148–10153. https://doi.org/10.1016/j.apsusc.2012.06.096.

Zhang, Y., Yang, Y., Han, H., et al., 2012. Ultra-deep desulfurization via reactive adsorption on Ni/ZnO: the effect of ZnO particle size on the adsorption performance. Appl. Catal. B Environ. 119, 13–19. https://doi.org/10.1016/j.apcatb.2012.02.004.

Zhang, Y., Yong, Y., Feng, L., et al., 2013. Improvement of adsorptive desulfurization performance of Ni/ZnO adsorbent by doping with Mn additive. Chin. J. Catal. 34 (1), 140–145. https://doi.org/10.1016/S1872-2067(11)60513-5.

Zhang, S., Plessow, P.N., Willis, J.J., et al., 2016. Dynamical observation and detailed description of catalysts under strong metal–support interaction. Nano Lett. 16 (7), 4528–4534. https://doi.org/10.1021/acs.nanolett.6b01769.

Zhang, L., Wang, J., Sun, Y., et al., 2017. Deep oxidative desulfurization of fuels by superbase-derived Lewis acidic ionic liquids. Chem. Eng. J. 328, 445–453. https://doi.org/10.1016/j.cej.2017.07.060.

Zhao, Y., Zhang, Z., Yang, C., et al., 2018. Critical role of water on the surface of ZnO in H_2S removal at room temperature. Ind. Eng. Chem. Res. 57 (45), 15366–15374. https://doi.org/10.1021/ACS.IECR.8B03431.

Zhao, J., Chai, Y., Liu, B., et al., 2019. The effect of hydrogen on thiophene catalytic removal over Ni/Al_2O_3. Catal. Commun. 119, 6–10. https://doi.org/10.1016/j.catcom.2018.10.007.

Zhao, W., Chizallet, C., Sautet, P., et al., 2019. Dehydrogenation mechanisms of methyl-cyclohexane on γ-Al_2O_3 supported Pt_{13}: impact of cluster ductility. J. Catal. 370, 118–129. https://doi.org/10.1016/j.jcat.2018.12.004.

Zhu, H., Yu, Y., Li, G., et al., 2019. Unraveling the Active site and mechanism for C–S bond activation in alumina-supported Pt catalysts: ab initio insights into catalytic desulfurization. J. Phys. Chem. C 124 (1), 446–458. https://doi.org/10.1021/acs.jpcc.9b08532.

Zhu, H., Li, X., Shi, N., et al., 2021. Density functional theory study of thiophene desulfurization and conversion of desulfurization products on the Ni(111) surface and Ni_{55} cluster: implication for the mechanism of reactive adsorption desulfurization over Ni/ZnO catalysts. Catal. Sci. Technol. 11 (4), 1615–1625. https://doi.org/10.1039/D0CY01523G.